

Area-Selective Atomic Layer Deposition of SiO₂ Using Acetylacetone as a Chemoselective Inhibitor in an ABC-Type Cycle

Alfredo Mameli,[†] Marc J. M. Merkkx,[†] Bora Karasulu,^{†,§} Fred Roozeboom,^{†,‡} Wilhelmus (Erwin) M. M. Kessels,[†] and Adriaan J. M. Mackus^{*,†,‡}

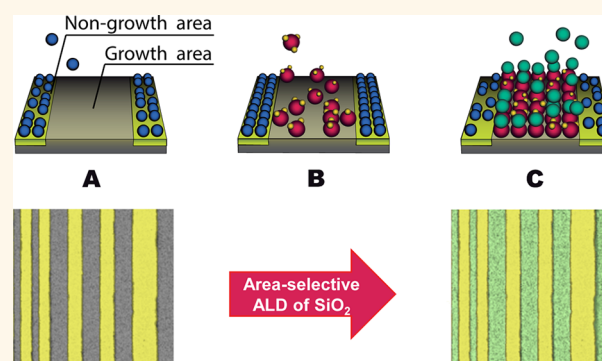
[†]Department of Applied Physics, Eindhoven University of Technology, P.O. Box 513, 5600 MB Eindhoven, The Netherlands

[‡]TNO-Holst Centre, High Tech Campus 31, 5656 AE Eindhoven, The Netherlands

S Supporting Information

ABSTRACT: Area-selective atomic layer deposition (ALD) is rapidly gaining interest because of its potential application in self-aligned fabrication schemes for next-generation nanoelectronics. Here, we introduce an approach for area-selective ALD that relies on the use of chemoselective inhibitor molecules in a three-step (ABC-type) ALD cycle. A process for area-selective ALD of SiO₂ was developed comprising acetylacetone inhibitor (step A), bis(diethylamino)silane precursor (step B), and O₂ plasma reactant (step C) pulses. Our results show that this process allows for selective deposition of SiO₂ on GeO₂, SiN_x, SiO₂, and WO₃, in the presence of Al₂O₃, TiO₂, and HfO₂ surfaces. *In situ* Fourier transform infrared spectroscopy experiments and density functional theory calculations underline that the selectivity of the approach stems from the chemoselective adsorption of the inhibitor. The selectivity between different oxide starting surfaces and the compatibility with plasma-assisted or ozone-based ALD are distinct features of this approach. Furthermore, the approach offers the opportunity of tuning the substrate-selectivity by proper selection of inhibitor molecules.

KEYWORDS: self-aligned fabrication, area-selective deposition, chemoselective inhibition, atomic layer deposition (ALD), silicon oxide, nanomanufacturing, density functional theory



Directing matter to create structures with atomic-level control of physical and chemical properties is a long sought-after goal in nanotechnology. The deposition of atoms at specific locations on a surface can boost advances in catalysis,^{1–3} energy harvesting,⁴ and semiconductor device fabrication.⁵ Today, the semiconductor industry is one of the main driving forces that pushes for advancing the field of area-selective deposition.^{6,7} As the state-of-the-art technology is entering the sub-10-nm scale, the conventional patterning of thin films is becoming extremely challenging in terms of atomic-scale precision and reliable processing. Current semiconductor manufacturing requires many lithography and etching steps to fabricate multilayered 3D devices with perfectly aligned features.⁸ Especially alignment issues leading to the so-called edge placement errors (EPEs) have become the prime bottleneck for continued downscaling.⁹ Therefore, innovative *bottom-up* techniques are required to replace or complement *top-down* fabrication schemes.

One of the main emerging solutions is to implement self-aligned fabrication schemes, in which a material is deposited on

a predetermined area in a selective manner. Area-selective deposition will reduce the number of photolithography and etching steps and thereby enable cost-effective options to create these structures in a bottom-up approach. Hence, a significant effort is underway in both industry and academia to develop robust area-selective deposition techniques.¹⁰

Atomic layer deposition (ALD) enables layer-by-layer growth with atomic-level thickness control. The technique relies on the cyclewise and alternate exposure of a substrate to various vapor-phase precursors that undergo self-limiting surface reactions, thereby allowing for uniform and 3D-conformal film deposition.¹¹ However, ALD typically leads to deposition on the entire surface, and therefore the process needs to be adapted to enable area-selective deposition.^{7,12–15} To date, most of the efforts in the field of area-selective ALD include substrate patterning steps before the area-selective ALD.^{12,16,17} On the

Received: July 5, 2017

Accepted: August 29, 2017

Published: August 29, 2017

other hand, in self-aligned fabrication, a partially processed device architecture is taken as the starting point, where patterning has been performed in a previous processing step. Thus, the sample surface consists of several different materials, and the challenge is to selectively deposit on the surface of only one or a subset of these materials. The area-selective ALD processes developed so far often concern metal-on-metal or oxide-on-oxide deposition.^{18–21} However, self-aligned fabrication can also require other material combinations to be deposited in an area-selective manner. For example, some applications might demand area-selective ALD on a specific metal oxide in the presence of other oxide surfaces.

In this work, an approach for area-selective ALD is introduced. It is based on a three-step (ABC-type) ALD cycle, where step A is the exposure of the surface to inhibitor molecules, and B and C are the steps of a regular ALD process. Earlier investigations in chemical vapor deposition illustrate some of the advantages of using inhibitors for achieving area-selective deposition.²² Our approach is inspired by the work of Yanguas-Gil *et al.*, who used inhibitor molecules (e.g., ethanol, acetone, hexane) in ABC-type ALD cycles to improve the doping efficiency in ALD-grown materials.²³ Instead of reducing the growth per cycle by partial blocking of the adsorption sites for the precursor molecule,²³ we intend to completely block precursor adsorption on specific starting materials.

Our approach for achieving area-selective ALD is illustrated in Figure 1. In step A, we use an inhibitor molecule that

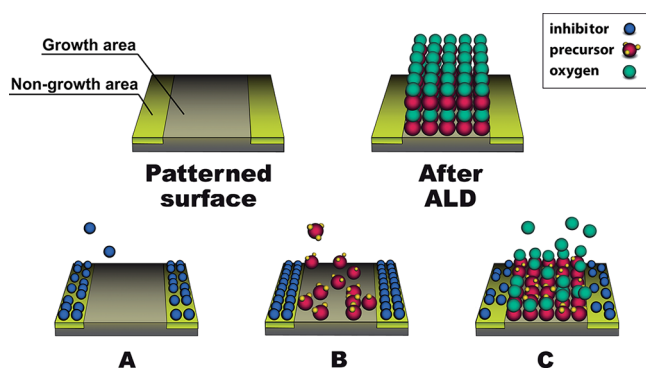


Figure 1. Schematic illustration of an ideal area-selective ALD process using ABC-type ALD cycles with inhibitor molecules. The starting point is a patterned surface with two different materials: the growth area on which selective deposition is desired, and the non-growth area on which deposition should not occur. In step A, the inhibitor molecules selectively adsorb on the non-growth area. These inhibitor molecules block the precursor adsorption in step B, such that precursor molecules adsorb only on the growth area. This results in area-selective deposition on the growth area after removal of the precursor ligands and inhibitor molecules in step C. By repeating the cycles, material can be deposited by ALD area-selectively. It should be noted that in reality some inhibitor adsorption could still be allowed on the growth area, provided the growth rate and/or material properties of the deposited film are not significantly affected.

selectively adsorbs on certain materials on which no deposition is desired (referred to as the non-growth area). The inhibitor blocks the precursor adsorption during the subsequent step B. The cycle is completed in step C by removing the precursor ligands together with the inhibitor molecules and by activating the surface for the next cycle. This approach should ideally

allow for area-selective ALD on surfaces where the inhibitor does not adsorb (referred to as the growth area).

A pronounced benefit of this approach is that the selectivity no longer relies solely on the chemoselective adsorption of an ALD precursor on a specific surface. Chemoselective adsorption is decoupled from the precursor by inserting an inhibitor step, and this will therefore yield more freedom for developing area-selective ALD processes. Similar to previous work on the application of self-assembled monolayers (SAMs) for area-selective ALD, this approach relies on the blocking of surface sites for precursor adsorption. However, the main difference is that the inhibitor molecules are reapplied every single cycle, which can potentially lead to a more robust approach that does not suffer from a gradual degradation of the blocking layer.¹³ Another advantage of reapplying the inhibitor every cycle is that it renders area-selective deposition compatible with (or accessible to) more types of ALD processes, including plasma-assisted or ozone-based ALD. This will therefore extend the set of materials that can be deposited by ALD in an area-selective manner.

In this article, we demonstrate a proof-of-concept for using ABC-type ALD cycles to achieve area-selective ALD of SiO₂, a low- κ material that is ubiquitous in many devices. The process consists of acetylacetone (abbreviated in the literature as Hacac) as the inhibitor, bis(diethylamino)silane (BDEAS) as the Si precursor, and O₂ plasma as the co-reactant. In contrast to previous area-selective ALD studies in which typically only two surfaces were considered, the nucleation behavior of this ABC-type ALD process is investigated here on as many as 14 different starting surfaces. As a proof-of-concept, the process was tested on patterned Al₂O₃/GeO₂ samples, and the selectivity was probed using surface analysis techniques. Theoretical calculations as well as *in situ* studies were performed to determine the mechanistic aspects of the chemoselective inhibitor adsorption and the precursor blocking. The basic understanding obtained this way can be used to further improve the selectivity of the current approach. Finally, the opportunities enabled by this area-selective ALD approach will be discussed.

RESULTS AND DISCUSSION

Impact of Hacac Adsorption on SiO₂ Nucleation.

Saturation curves for the ABC-type ALD cycle, included in the Supporting Information (Figure S1), demonstrate that the saturation behavior and the growth per cycle are not influenced by the addition of the Hacac step. ABC-type ALD cycles of SiO₂ were carried out on various starting surfaces to identify on which surfaces deposition of SiO₂ is obtained and on which ones it is blocked. Figure 2 depicts the nucleation curves as measured by *in situ* spectroscopic ellipsometry (SE). The graph shows that SiO₂ grows without any nucleation delay on GeO₂, SiO₂, WO₃, and SiN_x. On these substrates a growth per cycle of approximately 0.09 nm/cycle was obtained. This is comparable to the growth per cycle of the regular two-step ALD process, consisting of BDEAS precursor and O₂ plasma pulses (referred to as the BC process).²⁴ Figure 2 also shows that growth delays for ABC-type ALD of SiO₂ are observed on Al₂O₃ (15 cycles), TiO₂, and HfO₂ (both 10 cycles). The growth delay of 15 cycles that is obtained when using the ABC-type cycles on Al₂O₃ means that a SiO₂ film of ~1 nm thickness can be selectively deposited on GeO₂ in the presence of Al₂O₃. Nucleation curves for the BC process are shown in Figure S2, demonstrating that there is no nucleation delay for the regular

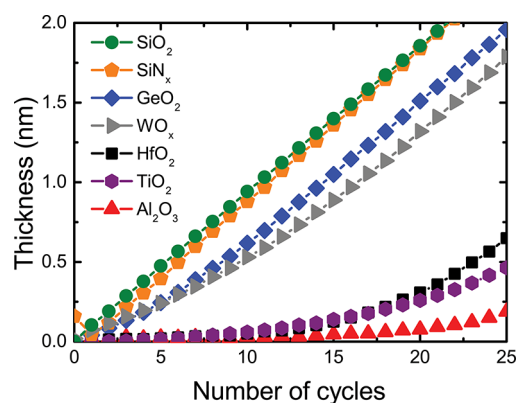


Figure 2. Nucleation curves for ABC-type ALD of SiO₂ on different starting surfaces. The graphs show the thickness as a function of the number of ALD cycles as measured by *in situ* SE. We note that due to the use of an O₂ plasma as the co-reactant, the topmost layer of the starting surfaces can be oxidized during the first few ALD cycles, which was accounted for in the SE modeling of SiN_x.

ALD process on these starting materials. Additional data for ABC-type ALD cycles of SiO₂ on Pd, Pt, Ru, ZnO, FeO_x, MoO_x, and CoO_x starting surfaces, presented in Figure S3a, show immediate deposition on Pd, short nucleation delays (of ~5 cycles) on Ru, ZnO, FeO_x, and Pt, and longer delays (of ~8–12 cycles) on MoO_x and CoO_x. Figure S3b depicts that the deposition temperature also plays a role in determining the extent of the nucleation delay, and slightly better results were obtained at 200 °C.

To gain insights into the inhibited deposition on Al₂O₃ and the immediate deposition on SiO₂, SE measurements were conducted after every individual subcycle. Figure 3a,b show the results for a sequence of AC, ABC, and BC cycles on Al₂O₃ and SiO₂ starting surfaces. Similar data are presented for other starting surfaces such as TiO₂, GeO₂, and HfO₂ in Figure S4. The data for the AC cycles on Al₂O₃ in Figure 3a show a thickness increase after each A step and a decrease after every subsequent C step. This suggests that Hacac adsorbs on Al₂O₃ and can be removed by an O₂ plasma pulse. The thickness increase does not correspond directly to the thickness of the Hacac monolayer, because its dielectric function is unknown and not taken into account in the SE modeling. However, the thickness increase can be considered as a measure for the amount of adsorbed material and is therefore represented as an *apparent thickness*.²⁵ Pulse C removes the adsorbed Hacac by combustion reactions and prepares the surface for the subsequent cycle. The thickness does not decrease completely to zero during the first O₂ plasma step, which is attributed to a slight change of the optical response of the underlying Al₂O₃ film affecting the ellipsometry modeling. The middle part of Figure 3a representing the ABC cycles indicates that after exposing the Al₂O₃ surface to Hacac (A), no significant amount of BDEAS adsorption takes place (B). Conversely, when exposing the Al₂O₃ surface to BDEAS (B) and O₂ plasma (C), as shown at the right-hand side in the graph, there is a net thickness increase indicating deposition of SiO₂ with a growth per cycle of ~0.09 nm/cycle.

Marked differences are observed when performing AC and ABC cycles on a SiO₂ substrate (Figure 3b). There is virtually no change in apparent thickness during AC cycles on SiO₂, which indicates that Hacac adsorbs, at most, in minute and ineffective amounts on a SiO₂ surface. Consequently, ABC-type

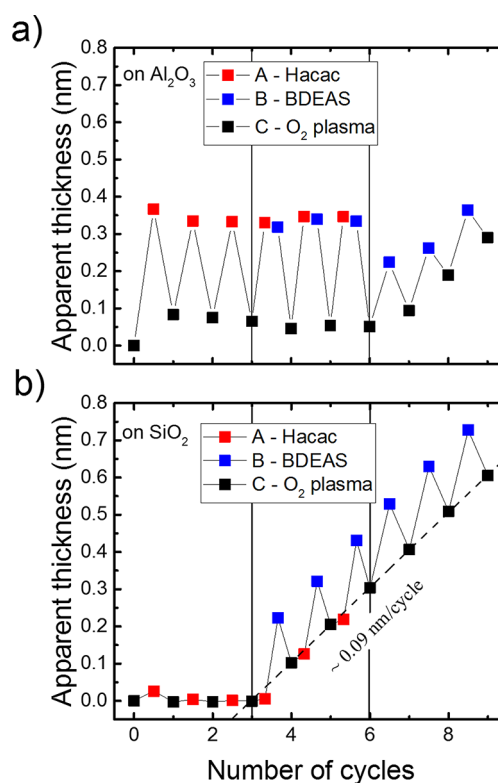


Figure 3. Apparent thickness as measured after every reactant dosing pulse on (a) Al₂O₃ and (b) SiO₂. The left-hand part of the figure represents 3 AC cycles with Hacac (A) and O₂ plasma (C) pulses, the middle part 3 ABC cycles with Hacac (A), BDEAS precursor (B), and O₂ plasma (C) pulses, and the right-hand part 3 BC cycles with BDEAS precursor (B) and O₂ plasma (C) pulses. The apparent thickness is used to reflect that the SE modeling did not take into account the dielectric function of the surface groups such that the thickness after step A might not correspond to the physical thickness.²⁵ The starting surfaces were prepared by regular ALD.

cycles on SiO₂ result in the same growth per cycle (~0.09 nm/cycle) as observed for regular ALD using BC cycles. This demonstrates that the addition of Hacac does not significantly influence the SiO₂ deposition on SiO₂ starting surfaces. To conclude, Figure 3 suggests that the selectivity of the ABC-type process stems from the chemoselective adsorption of Hacac and that Hacac—once adsorbed—effectively blocks the precursor adsorption.

Proof-of-Concept of Area-Selective Deposition. ABC-type ALD of SiO₂ was performed on Al₂O₃ and GeO₂ surfaces. GeO₂ was selected as a starting surface because it shows similar behavior to SiO₂; that is, the addition of an Hacac pulse to the cycle does not significantly affect the deposition of SiO₂ on this surface. Moreover, the GeO₂ surface allows for quantification of the amount of SiO₂ deposited using X-ray photoelectron spectroscopy (XPS) and time-of-flight secondary ion mass spectroscopy (TOF-SIMS). Figure S5 shows the Si 2p signals for SiO₂ after 12, 15, and 21 ABC-type ALD cycles of SiO₂ on both GeO₂ and Al₂O₃ starting surfaces. After 15 ABC-type ALD cycles the ratio of the Si 2p integrated peak areas on Al₂O₃ and GeO₂ is ~0.11. Consistent with the SE data, the integrated peak areas for the Si 2p peak confirm the blocking effect of Hacac.

The selectivity was further investigated on a patterned Al₂O₃/GeO₂ sample. To this end, an ALD-prepared Al₂O₃ layer

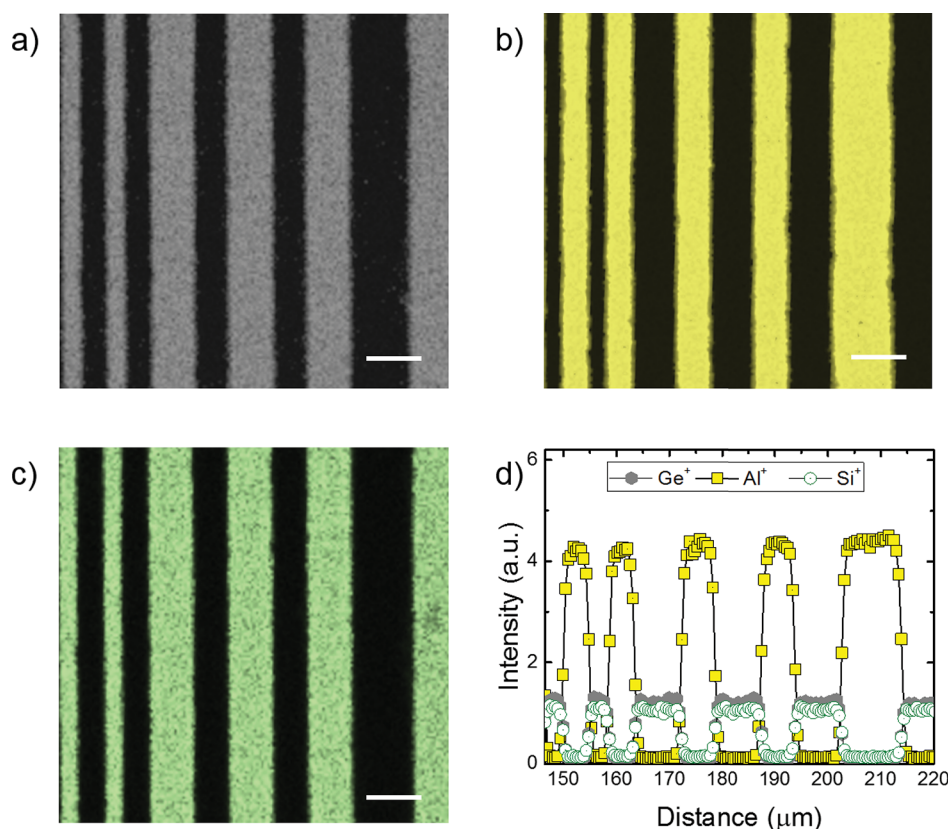


Figure 4. Elemental TOF-SIMS mappings showing (a) Ge^+ in gray, (b) Al^+ in yellow, and (c) Si^+ in green, after 15 SiO_2 ABC-type ALD cycles using Hacac as inhibitor; scale bar is 10 μm . (d) Corresponding line scans for Ge^+ , Al^+ , and Si^+ of the sample.

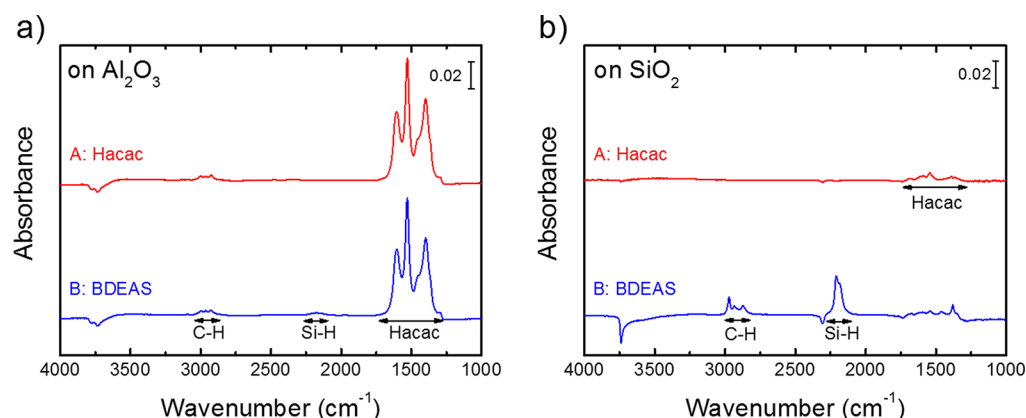


Figure 5. *In situ* infrared absorption spectra recorded after Hacac dosing (step A) and BDEAS precursor dosing (step B) during ABC-type ALD of SiO_2 on (a) an Al_2O_3 -coated substrate and (b) a SiO_2 -coated substrate. The graph for Al_2O_3 shows the adsorption of a large amount of Hacac and the blocking of BDEAS precursor adsorption during the subsequent pulse. The graph for SiO_2 reveals that only a small amount of Hacac adsorbs on SiO_2 , which does not significantly affect the adsorption of the BDEAS precursor. The spectra collected after steps A and B are both referenced to the starting surface (*i.e.*, Al_2O_3 and SiO_2).

was patterned on a GeO_2 surface using a regular lift-off method. Figure 4a–c show the TOF-SIMS elemental mapping images for the Ge^+ , Al^+ , and Si^+ secondary ions for the patterned sample after 15 ABC-type ALD cycles of SiO_2 . The mappings confirm that ALD of SiO_2 occurred predominantly on the GeO_2 regions. The line scans, presented in Figure 4d, show a high Si^+ signal in the regions not covered by Al_2O_3 , indicating area-selective deposition of SiO_2 on GeO_2 . Only a very small amount of Si is also present on Al_2O_3 , which was quantified to correspond to a 0.01 nm thick SiO_2 layer, as derived from calibration measurements (see the Methods section). Also,

lateral broadening of ~ 1 nm, the so-called *mushrooming effect*, is expected to take place given the nature of the ALD technique. This will mainly impact (and be observable for) nanoscale patterns, and the effect will be investigated on such samples in future work.

Surface Chemistry of the ABC SiO_2 ALD Process. In order to investigate the Hacac and BDEAS adsorption on SiO_2 and Al_2O_3 starting surfaces, *in situ* infrared absorption spectroscopy experiments were performed on pellet-pressed SiO_2 powder using a Fourier transformed spectrometer (FTIR). To this end, the SiO_2 powder was first coated using

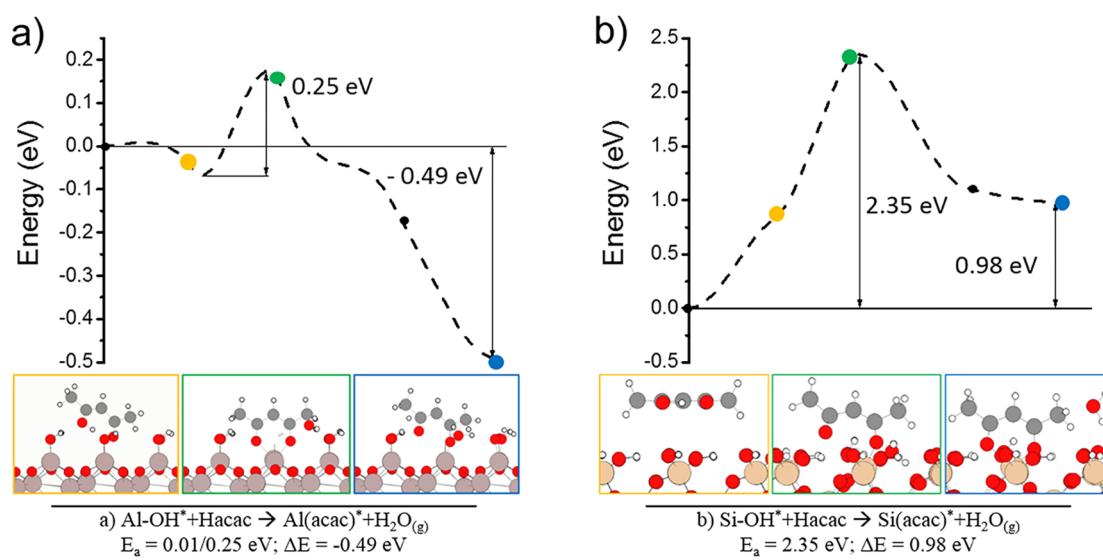


Figure 6. DFT (GGA/PBE-D3) level minimum energy paths for the Hacac adsorption on (a) Al_2O_3 and (b) SiO_2 surfaces, as described by the corresponding chemical equations. Minimum energy structures of the important steps are also shown (yellow, green, and blue dots and corresponding insets), where some oxygen and hydrogen atoms are hidden for clarity. First points of the energy profiles correspond to the Hacac species physisorbed on each surface and have $\Delta E_p = -0.75$ and -0.37 eV with respect to the separated Hacac gas phase and $\text{Al}_2\text{O}_3/\text{SiO}_2$ surfaces. These are taken as reference points (0 eV) to calculate the activation and final-state energies. Color code for atoms: silicon, pink; aluminum, light gray; hydrogen, white; oxygen, red; carbon, gray.

30 ALD cycles of SiO_2 or Al_2O_3 , respectively. FTIR spectra were collected after coating the powder and after the subsequent Hacac and the BDEAS dosing steps. Figure 5a shows the results on Al_2O_3 as difference spectra, using the spectrum collected after Al_2O_3 coating as the reference. The results confirm that Hacac adsorbs on Al_2O_3 , as indicated by the absorption peaks in the wavenumber range $1300\text{--}1650\text{ cm}^{-1}$.^{26,27} Subsequent dosing of BDEAS precursor causes only a minor change in the spectrum, which confirms that the preadsorbed Hacac molecules act as inhibitors and block the impinging BDEAS molecules from chemisorbing onto the Al_2O_3 surface. It is estimated that the minor change corresponds to a fraction of $\sim 8\%$ of the amount of BDEAS molecules adsorbed on bare Al_2O_3 . This indicates that Hacac is not fully effective in blocking the precursor adsorption.

A similar experiment on the SiO_2 -coated sample, using identical Hacac and BDEAS dosing times, revealed a distinctly different behavior, as shown in Figure 5b. Now, only 8% of Hacac adsorbs on SiO_2 as compared to the amount that adsorbs on the Al_2O_3 -coated surface. Consequently, the adsorption of BDEAS is not significantly affected on this surface, as shown by the large (positive) absorption peaks. BDEAS adsorption results in positive peaks in the wavenumber ranges $2800\text{--}3000\text{ cm}^{-1}$ and $2130\text{--}2240\text{ cm}^{-1}$, originating from the C–H and Si–H stretching vibrations of the adsorbed BDEAS molecules.^{28,29} Concurrently, there is a loss of absorbance around 3740 cm^{-1} , characteristic for the O–H stretching vibrations of the surface hydroxyl groups that are consumed during BDEAS precursor adsorption.^{28,30}

In conclusion, the FTIR studies confirm that Hacac selectively adsorbs on Al_2O_3 and subsequently inhibits the BDEAS adsorption. Yet, the studies also provide insights for further improvement of the process that will be discussed below.

Mechanism Underpinning the Chemoselective Adsorption of the Hacac Inhibitor. Density functional theory (DFT) calculations were performed to better understand the

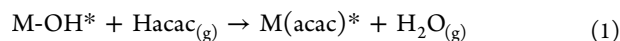
mechanism of the chemoselective Hacac adsorption at a molecular level. Hydroxylated surfaces of $\alpha\text{-Al}_2\text{O}_3$ (0001) and $\alpha\text{-SiO}_2$ (0001) were employed to represent the experimentally used Al_2O_3 and SiO_2 surfaces. The calculations revealed that Hacac prefers to bind in a chelate configuration on both surfaces, with both of its oxygen atoms bonded to $\text{Al}^{3+}/\text{Si}^{4+}$ surface sites. Alternative binding configurations were also found, as discussed below. Concertedly, H_2O is predicted to form as a byproduct on both surfaces through a proton transfer to a hydroxyl surface group. The H_2O byproduct is expected to stick to the surface, where it plays an important role in stabilizing the chemisorbed acac^- product through H-bond interactions (see Supporting Information, Figure S7 and the accompanying discussion).

The structures and associated relative energies were calculated for the stationary points along the suitable reaction pathways (*i.e.*, minimum energy paths) for the adsorption of the Hacac inhibitor on Al_2O_3 and SiO_2 (Figure 6). For the first step in Hacac binding, *i.e.*, physisorption, two distinctive binding orientations were identified by the DFT calculations (horizontal and vertical; see Figure S6 and detailed description in the Supporting Information). As evident from Figure 6a, the dissociative binding of Hacac on Al_2O_3 is associated with an overall exothermic reaction with an energy gain of 0.49 eV. The chemisorption involves the formation of an intermediate complex through a slightly exothermic ($\Delta E = -0.07$ eV) process with near-zero barrier ($E_a \approx 0.01$ eV). The intermediate complex comprises Hacac that is bonded to the Al^{3+} site through one of its oxygen atoms (Figure S7a). This intermediate species is predicted to lose its hydroxyl proton through a kinetically accessible process ($E_a = 0.25$ eV), producing a monodentate adduct (type A, Figure S7b) alongside H_2O . However, this adduct corresponds to a transition-state species on the energetically downhill path that yields the chelate end-product (type B, Figure S7c) through binding of acac^- via its second oxygen to the same surface Al^{3+} site. Considering that the Hacac would have already gained

sufficient kinetic energy by physisorbing on the Al_2O_3 surface (i.e., $\Delta E_p = -0.75$ eV, physisorption energy), it would readily overcome the overall barrier of 0.25 eV and be converted to the chelate (type B) end-product. Therefore, none of the monodentate (type A) species (intermediate or adduct) are expected to accumulate on the Al_2O_3 surface.

Similar to the Al_2O_3 case, a chelate (type B, Figure S7d) species is the end-product of Hacac adsorption on SiO_2 , whereas the monodentate (type A) complex is only a transition state (Figure 6b). More importantly, the overall chemisorption reaction on SiO_2 is calculated to be endothermic and to require an energy of 0.98 eV, accompanied by an extremely high kinetic barrier ($E_a = 2.35$ eV). In accordance with the SE and FTIR results, these DFT findings suggest that Hacac binds readily on hydroxylated Al_2O_3 , while the overall reaction on hydroxylated SiO_2 is both thermodynamically and kinetically hindered. This explains the selectivity of Hacac adsorption on Al_2O_3 as opposed to SiO_2 during the ABC-type ALD of SiO_2 .

Role of Surface Acidity on Hacac Adsorption. The chemoselective adsorption of Hacac on various starting surfaces can also be interpreted in terms of surface acidity.³¹ This allows explaining the results obtained on the experimentally used starting surfaces. Hacac has a $\text{p}K_a$ value of 9.0 in aqueous solution at 25 °C, and therefore it should behave as a weak acid.³² A reaction with Hacac is not likely to occur with the hydroxyl groups that possess an acidic character (e.g., SiO_2).³³ Conversely, hydroxyl groups with more basic character can react with Hacac. In this framework, an acid/base surface reaction between Hacac and the surface hydroxyl groups of a given oxide (e.g., Al_2O_3) can be written as



where M is a generic atom of the oxide (either metal or nonmetal) and the asterisks represent the surface species. A generalization can be made in order to explain which surfaces allow for the chemoselective adsorption of the Hacac inhibitor (and potential blocking of the precursor) and which surfaces will lead to immediate deposition instead. The acidity of an oxide can be predicted from the electronegativity of the cation element, M.³⁴ The relative acidity of several oxide surfaces was calculated using Sanderson's electronegativity scale and the electronegativity equalization principle, in order to explain the data of Figures 2 and S3, as presented in Figure S8. The agreement of the calculated values with the experimental data underlines that the distinct acidic/basic behavior of different oxide compounds governs the chemoselective adsorption of Hacac. Therefore, this provides a framework for predicting the area selectivity on different starting surfaces.

Merits and Opportunities Provided by the Approach.

The approach introduced in this article shows similarities with recent work by Engstrom and co-workers in which inhibitor molecules are co-injected into the reactor together with the precursor.³⁵ Also that approach relies on influencing the precursor adsorption by an inhibitor molecule. The benefit of dividing the inhibitor and precursor exposure over two different dosing steps is that the adsorption of both molecules can reach saturation independently, without suffering from competitive adsorption effects. Consequently, similar to regular two-step ALD processes, an ABC-type ALD process should allow for the deposition of conformal films on nanostructured surfaces.

A more natural approach for achieving area-selective ALD would be to design dedicated ALD precursors to enable chemoselective adsorption on materials on which deposition

should occur. However, in practice this is extremely challenging because the precursor molecule has to contain the atom to be deposited, while also satisfying other requirements to behave as an effective ALD precursor (in terms of stability, volatility, and self-limiting adsorption). By using two different molecules in an ABC-type ALD cycle, the inhibitor provides the selectivity in step A, without compromising the properties of the precursor dosed in step B.

When the ABC-type ALD approach is compared to other area-selective ALD approaches, several distinctive aspects can be identified. As discussed in the introduction, reapplying the inhibitor molecules every cycle can be beneficial from a reliability point-of-view, while it also makes the approach compatible with plasma-assisted or ozone-based ALD. Moreover, an important merit of this approach is that it distinguishes between the growth on different oxide surfaces (e.g., $\text{GeO}_2/\text{SiO}_2$ versus $\text{Al}_2\text{O}_3/\text{HfO}_2/\text{TiO}_2$).

The FTIR studies revealed that the selectivity of the Hacac adsorption is not perfect, since some adsorption was also observed on SiO_2 . However, the amount of Hacac on SiO_2 is sufficiently small such that it does not influence the deposition on the growth area, as we concluded from the *in situ* SE measurements (Figures 2 and S1). Moreover, a small amount of BDEAS adsorption was detectable on Al_2O_3 after dosing the Hacac inhibitor. *Ex situ* XPS and TOF-SIMS also confirmed that a minor amount of SiO_2 was deposited on Al_2O_3 after 15 cycles, suggesting that the adsorbed Hacac does not completely block the precursor adsorption. This incomplete precursor blocking can occur most likely due to the presence of (i) surface defects or impurities that can negatively influence the ideal inhibitor adsorption behavior; (ii) surface reactive sites that remain accessible to the precursor; and (iii) physisorbed water molecules on the surface that can compete with the Hacac chemisorption, as discussed in the DFT calculations in the Supporting Information, Figure S7. This implies that the selectivity of the ABC-type ALD process can be further improved by exploring different surface preparation procedures and by optimizing the deposition conditions. In addition, alternative inhibitors, different inhibitor dosing strategies, or co-dosing two or more inhibitor molecules can be considered for improving the selectivity. All these parameters offer physicochemical pathways to enhance the inhibitor surface coverage and, therefore, maximize the blocking effect during the precursor dose step. For these reasons, we foresee that it should be possible to significantly improve the selectivity to the extent it meets the requirements of semiconductor manufacturing.

The ABC approach provides the opportunity of tailoring the substrate-selectivity of an ALD process by selection of the chemoselective inhibitor molecule. There is a wealth of information in surface science and catalysis literature about the adsorption of organic molecules on inorganic surfaces,^{36,37} which can serve as a good starting point for selecting suitable inhibitor molecules.²³ The ideal case would be to use an inhibitor molecule that adsorbs on all surfaces, except for the particular surface on which deposition is needed. Additional research is required to investigate whether such selectivity is achievable and to further explore the toolbox of using inhibitor molecules for area-selective ALD. We expect that this approach can enable area-selective ALD for different materials by using other precursors and for example H_2 or NH_3 plasma co-reactants. To this end, the interaction of the inhibitor with the material to be deposited and with the plasma needs to be

studied. In view of the large set of possibilities, this will be the subject of a follow-up study.

CONCLUSIONS

We have demonstrated the use of chemoselective inhibitors in ABC-type ALD cycles as a route for area-selective ALD. Area-selective ALD of SiO₂ was achieved using a process consisting of alternated Hacac inhibitor, BDEAS precursor, and O₂ plasma pulses on a GeO₂ substrate with patterned Al₂O₃ features. SiO₂ is an extremely relevant and widely employed low- κ material, for which no area-selective ALD process is available. *In situ* SE studies revealed that area-selective (*i.e.*, noninhibited) growth can also be obtained on WO₃, SiO₂, SiN_x, and Pd, while there are nucleation delays of 10–15 cycles on TiO₂, HfO₂, CoO_x, and MoO_x. The selectivity originates from the chemoselective adsorption of the Hacac inhibitor molecule. This was corroborated in detail by *in situ* SE and FTIR experiments, as well as by DFT calculations, and generalized by correlating the Hacac adsorption to the acidity of the starting surface. SE and FTIR experiments confirmed that adsorbed Hacac blocks the subsequent BDEAS precursor adsorption, thereby resulting in area-selective deposition of SiO₂ on those surfaces on which Hacac does not adsorb.

The presented results establish a proof-of-concept for the introduced approach and provide insight into how the selectivity can be further improved. The SiO₂ ABC-type process offers an exceptional substrate-selectivity, by distinguishing between different oxide starting surfaces. We expect that the compatibility of the approach with ozone-based or plasma-assisted ALD, as well as the ability to tune the substrate-selectivity by selection of the inhibitor molecule, will extend the portfolio of materials that can be deposited by ALD in an area-selective manner.

METHODS

ALD Processes. The depositions were carried out in an Oxford Instruments FlexAL reactor, which is described in detail in ref 38. In short, it is a vacuum vessel equipped with a remote inductively coupled plasma (ICP) source, a 200 mm substrate table, a turbo-molecular pump, and a loadlock. The SiO₂ plasma-assisted ALD recipe with BDEAS (H₂Si[N(C₂H₅)₂]₂) precursor (also known as SAM.24) and O₂ plasma pulses, characterized by Dingemans *et al.*,²⁴ was used as the starting point. The recipe was changed to an ABC-type ALD process by adding a step of Hacac dosing before the precursor step. The Hacac ($\geq 99\%$ ReagentPlus; CAS 123-54-6) was purchased from Sigma-Aldrich, and it was employed without further purification. The Hacac has a vapor pressure of 6 Torr at 25 °C, and it exists in two tautomeric forms: keto and enol. In gas phase, the tautomeric equilibrium is shifted toward the enol form,³⁹ which was the form considered in the DFT calculations. The Hacac inhibitor was kept at room temperature in a stainless steel container and vapor drawn into the chamber using 3 pulses of 5 s each. All experiments were carried out at a substrate temperature of 150 °C.

Substrate Preparation Methods. A set of 14 different materials was investigated as starting surfaces in this study. Al₂O₃, HfO₂, TiO₂, WO₃, CoO_x, MoO_x, FeO_x, ZnO, Pt, Pd, Ru, and SiN_x samples were prepared by ALD in our lab using standard ALD recipes. In addition, crystalline Si and Ge substrates were used. All these substrates were cleaned by 5 min O₂ plasma exposure (8 mTorr O₂, 200 W) prior to the deposition, with the exception of SiN_x. Because of this O₂ plasma cleaning step, the Si and Ge substrates are referred to as SiO₂ and GeO₂, respectively, in this article.

Analytical Methods. *In situ* SE was performed using a J.A. Woollam M2000D ellipsometer as the main diagnostic technique to characterize the process and to measure the nucleation curves, using a Cauchy parametrization to model the data. In the case of SiN_x, O₂

plasma oxidation occurs during the SiO₂ deposition, which was taken into account in the modeling of the data of Figure 2. The nucleation delay was defined as the number of cycles until the first data point that showed a measurable increase in thickness. The dielectric function of a monolayer of adsorbed Hacac molecules was not taken into account, and the same Cauchy parametrization as used to describe the deposited SiO₂ was employed to model the subcycle SE data of Figures 3 and S4. In these results, the thickness obtained from modeling the data after Hacac exposure is therefore represented as an “apparent thickness”.

XPS measurements were performed using a K-Alpha system from Thermo Scientific. TOF-SIMS analysis was performed at Philips Innovation Laboratories using an Ion-ToF TOF-SIMS IV instrument, which was operated in positive mode to measure Al⁺ ($m/z = 27$), Si⁺ ($m/z = 28$), and Ge⁺ (sum of $m/z = 70, 72$ representing the most abundant isotopes of Ge). In addition, TOF-SIMS mapping was performed on patterned GeO₂/Al₂O₃ samples by applying burst-alignment with long pulses of 200 ns, resulting in high lateral resolution ($\sim 0.3 \mu\text{m}$), but low mass resolution ($\sim 1 m/z$). A series of 2, 5, and 10 regular ALD cycles for SiO₂ deposition was performed on Ge substrates to calibrate the TOF-SIMS signals for thickness quantification. These samples were probed using the high-current bunched mode, which allows for measurement with high mass resolution. Note that the thickness of the deposited SiO₂ on the GeO₂ regions is already beyond the linearity limit of TOF-SIMS, meaning that the ratio of the Si⁺ intensity of the GeO₂ and Al₂O₃ regions in the line scans underestimates the selectivity.

In situ FTIR experiments were carried out in a home-built ALD setup, which is very similar to the FlexAL reactor in terms of the plasma source and pumping system. This home-built setup is equipped with a Bruker Vector FTIR spectrometer with a mid-infrared light source (Globar $\sim 10\,000$ – $50\,000\text{ cm}^{-1}$) and a liquid N₂ cooled mercury cadmium telluride detector with a spectral range of $12\,000$ – 550 cm^{-1} , a translational and rotational sample manipulator, and KBr windows that can be isolated from the chamber with gate valves. FTIR measurements were performed on Aerosil OX50 SiO₂ powder that was pellet-pressed on a tungsten mesh. The powder was heated to 150 °C by passing a current through the mesh. To account for the accessible surface area of the powder, the spectra were normalized to the peak intensities of regular saturated TMA or BDEAS adsorption on the same sample before the Hacac dosing.

Computational Methods. All electronic structure calculations were performed using the projector-augmented wave function^{40,41} as implemented in Vienna *Ab Initio* Simulation Package (VASP v.5.3.5).^{42–44} First-principles calculations were carried out using the generalized gradient approximation to the DFT.^{45,46} Perdew–Burke–Ernzerhof (PBE) exchange–correlation functionals⁴⁷ were employed, and the van der Waals interactions were also accounted for on an empirical basis (PBE-D3).⁴⁸ Hydroxylated α -Al₂O₃ and α -SiO₂ clusters were used as approximations of the amorphous hydroxylated Al₂O₃ and SiO₂ used in the experiments. Additional computational details including the model system preparation can be found in the Supporting Information and also elsewhere.^{17,49}

ASSOCIATED CONTENT

Supporting Information

The Supporting Information is available free of charge on the ACS Publications website at DOI: 10.1021/acsnano.7b04701.

Additional characterization data, computational details, and supporting figures (PDF)

AUTHOR INFORMATION

Corresponding Author

*E-mail: a.j.mackus@tue.nl.

ORCID

Alfredo Mameli: 0000-0001-9175-8965

Bora Karasulu: 0000-0001-8129-8010

Wilhelmus (Erwin) M. M. Kessels: 0000-0002-7630-8226

Adriaan J. M. Mackus: 0000-0001-6944-9867

Present Address

[§]Department of Physics, University of Cambridge, Cavendish Laboratory, 19 J. J. Thomson Avenue, CB3 0HE, Cambridge, United Kingdom.

Notes

The authors declare no competing financial interest.

ACKNOWLEDGMENTS

This work was supported by Lam Research Corp. The work of A. Mameli was supported by TNO-Holst Centre (The Netherlands). The authors would like to thank K. Nardi, N. Draeger, D. Hausmann, and D. Smith (Lam Research) for valuable discussions, and J. Zeebregts, J. van Gerwen, C. van Helvoirt, J. Meulendijks, C. van Bommel, and T. de Vries for technical assistance.

REFERENCES

- (1) Cheng, N.; Banis, M. N.; Liu, J.; Riese, A.; Li, X.; Li, R.; Ye, S.; Knights, S.; Sun, X. Extremely Stable Platinum Nanoparticles Encapsulated in a Zirconia Nanocage by Area-Selective Atomic Layer Deposition for the Oxygen Reduction Reaction. *Adv. Mater.* **2015**, *27*, 277–281.
- (2) Xie, J.; Yang, X.; Han, B.; Shao-Horn, Y.; Wang, D. Site-Selective Deposition of Twinned Pt Nanoparticles on TiSi_2 Nanonets by Atomic Layer Deposition and Their Oxygen Reduction Activities. *ACS Nano* **2013**, *7*, 6337–6345.
- (3) Lee, H. B. R.; Baeck, S. H.; Jaramillo, T. F.; Bent, S. F. Growth of Pt Nanowires by Atomic Layer Deposition on Highly Ordered Pyrolytic Graphite. *Nano Lett.* **2013**, *13*, 457–463.
- (4) Li, R.; Zhang, F.; Wang, D.; Yang, J.; Li, M.; Zhu, J.; Zhou, X.; Han, H.; Li, C. Spatial Separation of Photogenerated Electrons and Holes among {010} and {110} Crystal Facets of BiVO_4 . *Nat. Commun.* **2013**, *4*, 1432.
- (5) Elko-Hansen, T. D.-M.; Dolocan, A.; Ekerdt, J. G. Atomic Interdiffusion and Diffusive Stabilization of Cobalt by Copper During Atomic Layer Deposition from Bis(N-Tert-Butyl-N'-Ethylpropionamido) Cobalt(II). *J. Phys. Chem. Lett.* **2014**, *5*, 1091–1095.
- (6) Fang, M.; Ho, J. C. Area-Selective Atomic Layer Deposition: Conformal Coating, Subnanometer Thickness Control, and Smart Positioning. *ACS Nano* **2015**, *9*, 8651–8654.
- (7) Kim, W.-H.; Minaye Hashemi, F. S.; Mackus, A. J. M.; Singh, J.; Kim, Y.; Bobb-Semple, D.; Fan, Y.; Kaufman-Osborn, T.; Godet, L.; Bent, S. F. A Process for Topographically Selective Deposition on 3D Nanostructures by Ion Implantation. *ACS Nano* **2016**, *10*, 4451–4458.
- (8) Pan, D. Z.; Liebmann, L.; Yu, B.; Xu, X.; Lin, Y. Pushing Multiple Patterning in Sub-10nm. *Proc. 52nd Annu. Des. Autom. Conf. - DAC '15* **2015**, 1–6.
- (9) Mulkens, J.; Hanna, M.; Wei, H.; Vaenkatesan, V.; Megens, H.; Slotboom, D. Overlay and Edge Placement Control Strategies for the 7nm Node Using EUV and ArF Lithography. *Proc. SPIE* **2015**, 9422, 94221Q.
- (10) Liddle, J. A.; Gallatin, G. M. Nanomanufacturing: A Perspective. *ACS Nano* **2016**, *10*, 2995–3014.
- (11) George, S. M. Atomic Layer Deposition: An Overview. *Chem. Rev.* **2010**, *110*, 111–131.
- (12) Mackus, A. J. M.; Bol, A. A.; Kessels, W. M. M. The Use of Atomic Layer Deposition in Advanced Nanopatterning. *Nanoscale* **2014**, *6*, 10941–10960.
- (13) Minaye Hashemi, F. S.; Prasittichai, C.; Bent, S. F. Self-Correcting Process for High Quality Patterning by Atomic Layer Deposition. *ACS Nano* **2015**, *9*, 8710–8717.
- (14) Heyne, M. H.; de Marneffe, J.-F.; Delabie, A.; Caymax, M.; Neyts, E. C.; Radu, I.; Huyghebaert, C.; De Gendt, S. Two-Dimensional WS_2 Nanoribbon Deposition by Conversion of Pre-Patterned Amorphous Silicon. *Nanotechnology* **2017**, *28*, 04LT01.
- (15) Lemaire, P. C.; King, M.; Parsons, G. N. Understanding Inherent Substrate Selectivity during Atomic Layer Deposition: Effect of Surface Preparation, Hydroxyl Density, and Metal Oxide Composition on Nucleation Mechanisms during Tungsten ALD. *J. Chem. Phys.* **2017**, *146*, 052811.
- (16) Chen, R.; Bent, S. F. Chemistry for Positive Pattern Transfer Using Area-Selective Atomic Layer Deposition. *Adv. Mater.* **2006**, *18*, 1086–1090.
- (17) Mameli, A.; Kuang, Y.; Aghaee, M.; Ande, C. K.; Karasulu, B.; Creatore, M.; Mackus, A. J. M.; Kessels, W. M. M.; Roozeboom, F. Area-Selective Atomic Layer Deposition of In_2O_3 :H Using a μ -Plasma Printer for Local Area Activation. *Chem. Mater.* **2017**, *29*, 921–925.
- (18) Mayberry, M. ALD: Essential but Not Sufficient. 15th International Conference on Atomic Layer Deposition, 2015.
- (19) Haider, A.; Yilmaz, M.; Deminsky, P.; Eren, H.; Biyikli, N. Nanoscale Selective Area Atomic Layer Deposition of TiO_2 Using E-Beam Patterned Polymers. *RSC Adv.* **2016**, *6*, 106109–106119.
- (20) Kamcev, J.; Germack, D. S.; Nykypanchuk, D.; Grubbs, R. B.; Nam, C. Y.; Black, C. T. Chemically Enhancing Block Copolymers for Block-Selective Synthesis of Self-Assembled Metal Oxide Nanostructures. *ACS Nano* **2013**, *7*, 339–346.
- (21) Lee, H.-B.-R.; Kim, H. Area Selective Atomic Layer Deposition of Cobalt Thin Films. *ECS Trans.* **2008**, *16*, 219–225.
- (22) Babar, S.; Mohimi, E.; Trinh, B.; Girolami, G. S.; Abelson, J. R. Surface-Selective Chemical Vapor Deposition of Copper Films through the Use of a Molecular Inhibitor. *ECS J. Solid State Sci. Technol.* **2015**, *4*, N60–N63.
- (23) Yanguas-Gil, A.; Libera, J. A.; Elam, J. W. Modulation of the Growth Per Cycle in Atomic Layer Deposition Using Reversible Surface Functionalization. *Chem. Mater.* **2013**, *25*, 4849–4860.
- (24) Dingemans, G.; van Helvoirt, C. A. A.; Pierreux, D.; Keuning, W.; Kessels, W. M. M. Plasma-Assisted ALD for the Conformal Deposition of SiO_2 : Process, Material and Electronic Properties. *J. Electrochem. Soc.* **2012**, *159*, H277–H285.
- (25) Langereis, E.; Heil, S. B. S.; Knoops, H. C. M.; Keuning, W.; van de Sanden, M. C. M.; Kessels, W. M. M. *In Situ* Spectroscopic Ellipsometry as a Versatile Tool for Studying Atomic Layer Deposition. *J. Phys. D: Appl. Phys.* **2009**, *42*, 073001.
- (26) van Veen, J. A. R.; Jonkers, G.; Hesselink, W. H. Interaction of Transition-Metal Acetylacetonates with $\gamma\text{-Al}_2\text{O}_3$ Surfaces. *J. Chem. Soc., Faraday Trans. 1* **1989**, *85*, 389–413.
- (27) Slabzhennikov, S. N.; Ryabchenko, O. B.; Kuarton, L. A. Interpretation of the IR Spectra of Aluminum, Gallium, and Indium Tris(acetylacetonates). *Russ. J. Coord. Chem.* **2006**, *32*, 545–551.
- (28) Stuart, B. H. *Infrared Spectroscopy: Fundamentals and Applications*; Ande, D. J., Ed.; Wiley: Dartford, Kent, UK, 2004.
- (29) Bugaev, K. O.; Zelenina, A. A.; Volodin, V. A. Vibrational Spectroscopy of Chemical Species in Silicon and Silicon-Rich Nitride Thin Films. *Int. J. Spectrosc.* **2012**, *2012*, 1–5.
- (30) Morrow, B. A.; Cody, I. A. Infrared Spectra of the Isolated Hydroxyl Groups on Silica. *J. Phys. Chem.* **1973**, *77*, 1465–1469.
- (31) Kytokivi, A.; Rautiainen, A.; Root, A. Reaction of Acetylacetonate Vapour with γ -Alumina. *J. Chem. Soc., Faraday Trans.* **1997**, *93*, 4079–4084.
- (32) The IUPAC Stability Constants Database, SC-Database and Mini-SCDatabase.
- (33) *Semiconductor Device-Based Sensors for Gas, Chemical, and Biomedical Applications*; Ren, F.; Pearton, S. J., Eds.; CRC Press: Boca Raton, USA, 2011.
- (34) Jeong, N. C.; Lee, J. S.; Tae, E. L.; Lee, Y. J.; Yoon, K. B. Acidity Scale for Metal Oxides and Sanderson's Electronegativities of Lanthanide Elements. *Angew. Chem., Int. Ed.* **2008**, *47*, 10128–10132.
- (35) Engstrom, J. R. Examination of the Mechanisms Involved in Self-Aligned, Selective Area Atomic Layer Deposition Using Surface Sensitive Probes. In *Area Selective Deposition Workshop*; Leuven, Belgium, 2016.

- (36) Ma, Z.; Zaera, F. Organic Chemistry on Solid Surfaces. *Surf. Sci. Rep.* **2006**, *61*, 229–281.
- (37) Barteau, M. A. Organic Reactions at Well-Defined Oxide Surfaces. *Chem. Rev.* **1996**, *96*, 1413–1430.
- (38) Heil, S. B. S.; van Hemmen, J. L.; Hodson, C. J.; Singh, N.; Klootwijk, J. H.; Roozeboom, F.; van de Sanden, M. C. M.; Kessels, W. M. M. Deposition of TiN and HfO₂ in a Commercial 200mm Remote Plasma Atomic Layer Deposition Reactor. *J. Vac. Sci. Technol., A* **2007**, *25*, 1357–1366.
- (39) Fokendt, M. M.; Weiss-Lopez, B. E.; Chauvel, J. P.; True, N. S. Gas-Phase ¹H Studies of Keto-Enol Tautomerism of Acetylacetone, Methyl Acetoacetate, and Ethyl Acetoacetate. *J. Phys. Chem.* **1985**, *89*, 3347–3352.
- (40) Blöchl, P. E. Projector Augmented-Wave Method. *Phys. Rev. B: Condens. Matter Mater. Phys.* **1994**, *50*, 17953–17979.
- (41) Kresse, G. From Ultrasoft Pseudopotentials to the Projector Augmented-Wave Method. *Phys. Rev. B: Condens. Matter Mater. Phys.* **1999**, *59*, 1758–1775.
- (42) Kresse, G.; Hafner, J. *Ab Initio* Molecular Dynamics for Liquid Metals. *Phys. Rev. B: Condens. Matter Mater. Phys.* **1993**, *47*, 558–561.
- (43) Kresse, G.; Hafner, J. *Ab Initio* Molecular-Dynamics Simulation of the Liquid-Metal–amorphous-Semiconductor Transition in Germanium. *Phys. Rev. B: Condens. Matter Mater. Phys.* **1994**, *49*, 14251–14269.
- (44) Kresse, G.; Furthmüller, J. Efficiency of *Ab-Initio* Total Energy Calculations for Metals and Semiconductors Using a Plane-Wave Basis Set. *Comput. Mater. Sci.* **1996**, *6*, 15–50.
- (45) Hohenberg, P. Inhomogeneous Electron Gas. *Phys. Rev.* **1964**, *136*, B864–B871.
- (46) Kohn, W.; Sham, L. J. Self-Consistent Equations Including Exchange and Correlation Effects. *Phys. Rev.* **1965**, *140*, A1133–A1138.
- (47) Perdew, J. P.; Burke, K.; Ernzerhof, M. Generalized Gradient Approximation Made Simple. *Phys. Rev. Lett.* **1997**, *78*, 1396–1396.
- (48) Grimme, S.; Antony, J.; Ehrlich, S.; Krieg, H. A Consistent and Accurate *Ab Initio* Parametrization of Density Functional Dispersion Correction (DFT-D) for the 94 Elements H–Pu. *J. Chem. Phys.* **2010**, *132*, 154104.
- (49) Kuang, Y.; Macco, B.; Karasulu, B.; Ande, C. K.; Bronsveld, P. C. P.; Verheijen, M. A.; Wu, Y.; Kessels, W. M. M.; Schropp, R. E. I. Towards the Implementation of Atomic Layer Deposited In₂O₃:H in Silicon Heterojunction Solar Cells. *Sol. Energy Mater. Sol. Cells* **2017**, *163*, 43–50.